

# Spotlight on Charge-Transfer Excitons in Crystalline Textured *n*-Alkyl Anilino Squaraine Thin Films

Frank Balzer, Nicholas J. Hestand, Jennifer Zablocki, Gregor Schnakenburg, Arne Lützen, and Manuela Schiek\*



Cite This: *J. Phys. Chem. C* 2022, 126, 13802–13813



Read Online

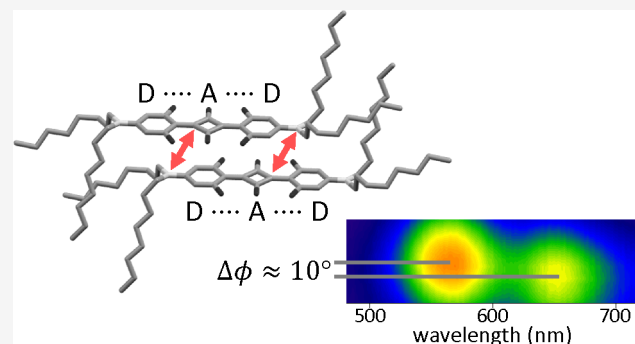
ACCESS |

Metrics & More

Article Recommendations

Supporting Information

**ABSTRACT:** Prototypical *n*-alkyl-terminated anilino squaraines for photovoltaic applications show characteristic double-hump absorption features peaking in the green and deep-red spectral range. These signatures result from the coupling of an intramolecular Frenkel exciton and an intermolecular charge-transfer exciton. Crystalline, textured thin films suitable for polarized spectromicroscopy have been obtained for compounds with *n*-hexyl (*n*HSQ) and *n*-octyl (*n*OSQ) terminal alkyl chains. The here-released triclinic crystal structure of *n*OSQ is similar to the known *n*HSQ crystal structure. Consequently, crystallites from both compounds show equal pronounced linear dichroism with two distinct polarization directions. The difference in the polarization angle between the two absorbance maxima cannot be derived by spatial considerations from the crystal structure alone but requires theoretical modeling. Using an essential state model, the observed polarization behavior was discovered to depend on the relative contributions of the intramolecular Frenkel exciton and the intermolecular charge-transfer exciton to the total transition dipole moment. For both *n*HSQ and *n*OSQ, the contribution of the charge-transfer exciton to the total transition dipole moment was found to be small compared to the intramolecular Frenkel exciton. Therefore, the net transition dipole moment is largely determined by the intramolecular component, resulting in a relatively small mutual difference between the polarization angles. Ultimately, the molecular alignment within the microtextured crystallites can be deduced, and with that, the excited-state transitions can be spotted.



## INTRODUCTION

Squaraine dyes are an attractive class of donor–acceptor–donor-type molecular semiconductors that have been used in a variety of applications.<sup>1–6</sup> Because their solid-state absorption and solute-state fluorescence are strong in the visible to near-infrared region, their purpose as a p-type material ranges from solar cells<sup>7–11</sup> and photosensors,<sup>12–15</sup> even in biological environments,<sup>16</sup> to thin film transistors<sup>17</sup> as well as photosensitizers in photodynamic therapy<sup>18,19</sup> and fluorescent labels.<sup>20,21</sup> Functionality typically arises from supramolecular interactions giving rise to new phenomena not present on a molecular level. Therefore, it is essential to understand molecular aggregation for the targeted design of optoelectronic and photonic applications. Aggregation both in colloidal solute systems and structured or extended thin films also requires comprehension from a theoretical perspective.<sup>22–29</sup>

Anilino squaraines (SQs), consisting of two anilino rings connected via a central squaric moiety, are of the donor–acceptor–donor (DAD) type: the molecular backbone is coplanarized by intramolecular hydrogen bonding if four hydroxy groups attached to the anilino rings are adjacent to the central core (Figure 1). The degenerate zwitterionic resonance

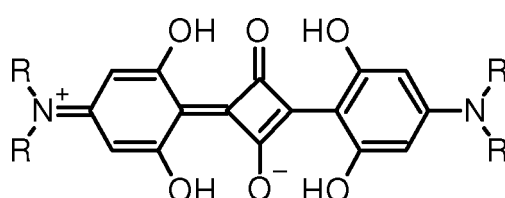


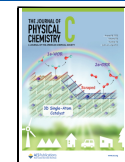
**Figure 1.** Schematic molecular structure of *n*-alkyl anilino squaraines in a zwitterionic resonance formula, where R denotes the variable alkyl substituents. In this study, these are linear alkyl chains of four, five, six, and eight carbon atoms: *n*-butyl (*n*BSQ), *n*-pentyl (*n*PSQ), *n*-hexyl (*n*HSQ), and *n*-octyl (*n*OSQ).

structures result in the quadrupolar character of the molecule and in a strong intramolecular charge transfer. This leads to

Received: May 27, 2022

Revised: July 22, 2022

Published: August 3, 2022



intense intermolecular interactions involving excitonic coupling in the aggregated state. Terminal alkyl substituents are not part of the chromophoric system; however, they steer the molecular packing and are thereby determinative of the excitonic coupling.

For example, bulky terminal functionalization leads to herringbone-like monoclinic and orthorhombic crystal phases.<sup>30,31</sup> Because their primitive unit cells contain more than one molecule, the optical thin-film absorbance spectra are typically dominated by Davydov splitting, which can be sufficiently explained by a classical Frenkel exciton picture.<sup>32</sup> In contrast, for linear *n*-alkyl substitution, triclinic crystal structures have been reported with only a single molecule per unit cell.<sup>11,33–36</sup> This excludes Davydov splitting as the reason for the absorbance spectra consisting of two broad spectral features. In this case, short intermolecular distances based on the slipped π-stacking allow for a pronounced intermolecular charge transfer (ICT). On the basis of theoretical modeling<sup>35,37</sup> it has been shown that coupling between this ICT resonance and an intramolecular Frenkel exciton results in the double-humped absorbance spectra.<sup>35,37</sup> The modeling of such spectra is generally based on the single-crystal structural data. Therefore, this has been limited for the *n*-alkyl SQs to compounds with alkyl chain lengths of three (nPrSQ), four (nBSQ), and six (nHSQ) carbon atoms until now.

Here, we provide the crystal structure of nOSQ, which is *n*-octyl SQ with eight carbon atoms. Together with the recently published crystal structure of nPSQ<sup>36</sup> (*n*-pentyl SQ, five carbon atoms), the impact of the ICT on the optical spectra can be quantified for the series nBSQ, nPSQ, nHSQ, and nOSQ. Upon spin-coating, these compounds were shown to form extended pseudouniaxial thin films with the crystallographic {0 0 1} plane parallel to the substrate but effectively random in-plane orientation.<sup>30</sup> Crystallites of sizes suitable for spectromicroscopy could also be obtained for nHSQ and nOSQ via drop casting or dip coating, and these samples exhibited an interesting polarization dependence of the high- and low-energy peaks. A previously established essential state model that includes ICT<sup>35,37</sup> is used to account for the distinct linear dichroism of textured, microcrystalline samples. The calculated spectra reproduce well the measured polarized absorbance spectra of such ordered nHSQ and nOSQ thin film samples. The key to resolving the spatial polarization pattern with respect to the micromorphology is to account for the relative contributions of the intramolecular Frenkel and intermolecular charge-transfer excitons to the total transition dipole moment of the absorbing states.

## METHODS

**Experimental Section.** *n*-Alkyl-terminated anilino squaraines nHSQ and nOSQ have been synthesized via a catalyst-free condensation reaction as previously documented.<sup>11,36</sup>

The single-crystal structures of nBSQ, nPSQ (CCDC code 1987522), and nHSQ (CCDC code 962720) have already been published.<sup>11,35,36</sup> Their crystallographic parameters are presented in Table S3 in the Supporting Information together with the parameters of the newly determined nOSQ (CCDC code 2077835) single-crystal structure. All unit cells adopt the space group P1. Single crystals of nOSQ were grown by vapor diffusion using dichloromethane as the solvent and cyclohexane as the antisolvent within 1 month.<sup>38</sup> The structural data of nOSQ were measured with a Bruker D8-Venture diffractometer at 166 K using Cu Kα radiation ( $\lambda = 1.54184$

Å). For data analysis, SHELXL version 2014/7 and OLEX2 including twinned data refinement have been used.<sup>39,40</sup> Lattice parameters for nOSQ are triclinic, space group P1,  $a = (5.3556 \pm 0.0004)$  Å,  $b = (10.7619 \pm 0.0006)$  Å,  $c = (19.5626 \pm 0.0012)$  Å,  $\alpha = (86.503 \pm 0.005)^\circ$ ,  $\beta = (89.667 \pm 0.005)^\circ$ ,  $\gamma = (78.726 \pm 0.005)^\circ$ , and  $Z = 1$ .

Crystal dimensions 0.600 mm × 0.400 mm × 0.200 mm; metallic bluish-green plate; empirical formula  $C_{48}H_{76}N_2O_2$ ; weight 777.10 amu;  $V = (1103.68 \pm 0.12)$  Å<sup>3</sup>; density 1.169 g/cm<sup>3</sup>; absorption coefficient 0.592 mm<sup>-1</sup>;  $F(000) = 426$ ; multiscan absorption correction (Bruker TWINABS-2012/1); 2θ range for data collection 4.526–129.988°; index ranges  $-6 \leq h \leq 6$ ,  $-12 \leq k \leq 12$ , and  $-22 \leq l \leq 22$ ; 7728 reflections collected; final  $R$  indices ( $I > 2\sigma(I)$ )  $R_1 = 0.1452$ ,  $wR_2 = 0.3551$ ;  $R$  indices (all data)  $R_1 = 0.2371$ ,  $wR_2 = 0.0.3997$ ; full-matrix least-squares on  $F^2$  refinement; GOF on  $F^2 = 1.158$  for 7728 data points and 0 restraint and 258 parameters; and largest diff. peak and hole 0.62 and  $-0.50$  eÅ<sup>-3</sup>, respectively.

Microcrystalline samples supported on objective slides (VWR float glass) have been obtained by drop casting or dip coating for nHSQ and nOSQ. The other compounds nBSQ and nPSQ showed less of a tendency to crystallize under these conditions and rather formed extended pseudouniaxial thin films.<sup>30</sup> To drop cast, a few drops of an ~1 mg/mL solution of nHSQ or nOSQ in amylene-stabilized chloroform were left to dry under ambient conditions for 1 to 2 h. For dip coating, a glass slide was placed upright standing in a slim beaker filled with an ~0.1 mg/mL solution of nHSQ or nOSQ in amylene-stabilized chloroform. The solvent was left to evaporate for 1 to 2 days under ambient conditions. The samples have been dried on a hot plate at 100 °C under inert nitrogen-filled glovebox conditions for 30 min.

X-ray diffraction (XRD) provided that for nHSQ and nOSQ and also for nBSQ and nPSQ the {0 0 1} face was parallel to the substrate.<sup>36</sup> Views of the molecular arrangements along the [1 0 0] direction and parallel to the (0 0 1) plane for nBSQ, nPSQ, nHSQ, and nOSQ are presented in Figure S1, and the top view onto the (0 0 1) planes for nHSQ and nOSQ is provided in Figure S2. The stacking direction for all molecules is the [1 0 0] direction. Polarized reflection microscope images of spin-cast nHSQ and nOSQ films together with unpolarized absorbance spectra (beam diameter ~3 mm) are shown in Figure S3 in the Supporting Information.

The morphology of the samples was determined by atomic force microscopy (AFM, JPK NanoWizard) in intermittent contact mode (Tap300-G BudgetSensors cantilevers). For AFM image analysis, Gwyddion has been used.<sup>41</sup>

Polarized optical microscopy is carried out with a Leica DMRME polarization microscope in either reflection or transmission. Spectral resolution is obtained by bandpass filters (Thorlabs FKB-VIS-10, fwhm 10 nm) in the beam path. The sample is rotated by a computer-controlled stage (Thorlabs PRM1Z8), whereas the directions of the linear polarizers in the microscope, either a single one or two crossed polarizers, are fixed. The polarization angle  $\phi_{\max}^{r,t}$  for which the reflectivity ( $r$ ) or the transmission ( $t$ ) is largest, is found pixelwise via a discrete Fourier transform using ImageJ (Supporting Information).<sup>42–45</sup> For fiber-like crystallites, also the angle  $\beta^{r,t}$  between the polarization angle  $\phi_{\max}^{r,t}$  and the long fiber axis is determined in reflection and transmission modes.<sup>46–49</sup> For spatially resolved polarized spectroscopy, a fiber-optics miniature spectrometer (Ocean Optics Maya2000) is coupled through a 200 μm optical fiber to the camera port of

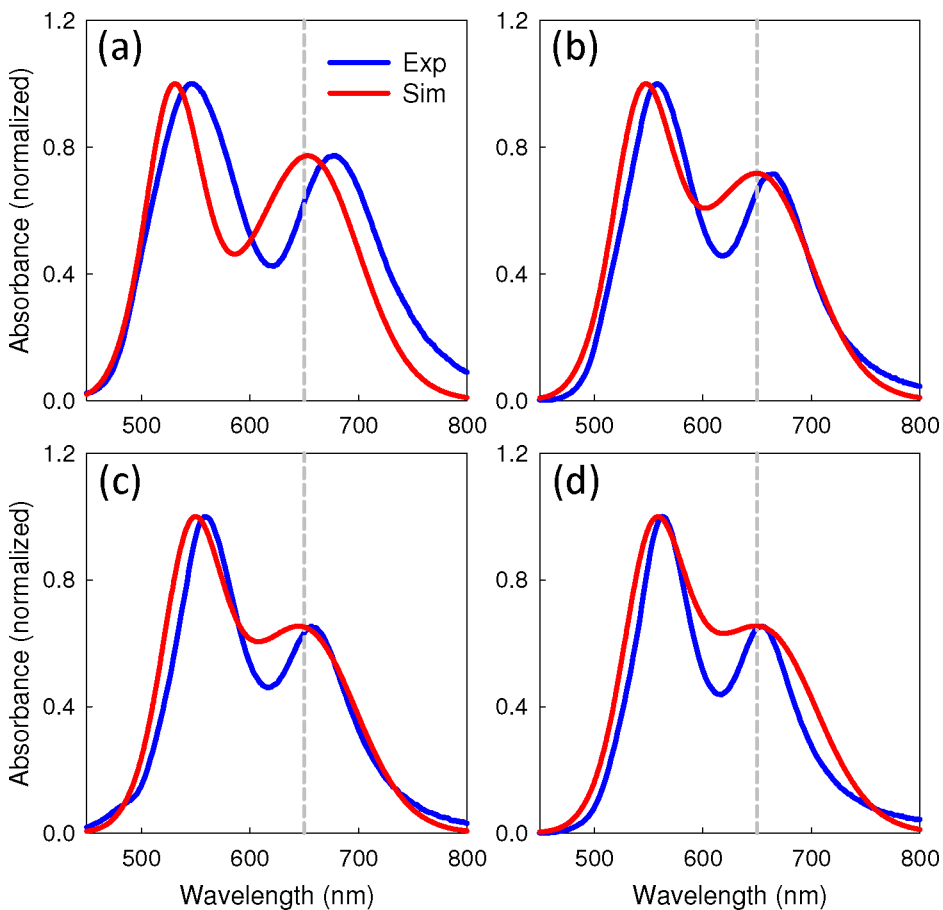


**Figure 2.** Simulated unpolarized absorbance spectra (red) compared to experiment (blue) for (a) nBSQ, (b) nPSQ, (c) nHSQ, and (d) nOSQ. Spectra were measured on spin-cast samples subjected to subsequently annealing at 120 °C. The dashed gray lines indicate the maximum absorbance of dissolved, nonaggregated molecules in a chloroform solution.<sup>36</sup>

the microscope. That way, light is collected from a spot of typically 30 to 70  $\mu\text{m}$  diameter, depending on the choice of the collection optics in front of the fiber and the magnification of the microscope objective.

**Modeling.** The absorbance spectra of the four compounds (nBSQ, nPSQ, nHSQ, and nOSQ) are modeled using an extended version of Painelli's essential states model for DAD chromophores.<sup>50,51</sup> In the essential states model, each molecule is modeled as a collection of three essential states that correspond to the molecule's dominant resonance structures: the state  $|\text{N}\rangle$  describes the neutral DAD structure, and the two degenerate states  $|\text{Z}_1\rangle$  and  $|\text{Z}_2\rangle$  describe the zwitterionic structures  $\text{D}^+\text{A}^-\text{D}$  and  $\text{DA}^-\text{D}^+$ , respectively.<sup>50</sup> The zwitterionic states lie higher in energy than the neutral state by  $\eta_Z$  and couple to the neutral state through  $-t_Z$ .

In ref 35, Painelli's model was extended to include ICT interactions to explain the double-hump absorption spectra observed for extended squaraine thin films. ICT between nearest-neighbor molecules is incorporated by including the ionic states  $|\text{A}\rangle$  ( $\text{DA}^-\text{D}$ ),  $|\text{C}_1\rangle$  ( $\text{D}^+\text{AD}$ ),  $|\text{C}_2\rangle$  ( $\text{DAD}^+$ ), and  $|\text{Z}_3\rangle$  ( $\text{D}^+\text{A}^-\text{D}^+$ ). Charge-transfer configurations of a dimer pair consisting of one molecule in the  $|\text{A}\rangle$  state and the other in either the  $|\text{C}_1\rangle$  or  $|\text{C}_2\rangle$  state are energetically offset from the state where both molecules are in the  $|\text{N}\rangle$  state by the ion pair energy  $\eta_{\text{CT}}$ . When one molecule is in the  $|\text{A}\rangle$  state and the other is in the  $|\text{Z}_3\rangle$  state, the energy is offset by an additional amount  $\eta_Z$ . The neutral molecular states  $|\text{N}\rangle$ ,  $|\text{Z}_1\rangle$ , and  $|\text{Z}_2\rangle$  couple to the ionic states  $|\text{A}\rangle$ ,  $|\text{C}_1\rangle$ ,  $|\text{C}_2\rangle$ , and  $|\text{Z}_3\rangle$  through the

ICT integral,  $-t_{\text{CT}}$ , which accounts for the transfer of an electron between a donor on one molecule and the acceptor on its neighbor. Hence, the two parameters describing ICT are  $-t_{\text{CT}}$  and  $\eta_{\text{CT}}$ .

Coulombic intermolecular interactions are included by allowing molecules to interact electrostatically when in zwitterionic or ionic states, and vibronic coupling is considered by treating each arm of the squaraine molecule as a harmonic oscillator whose equilibrium geometry depends on the electronic state of the molecule. Complete details of the model Hamiltonian can be found in ref 35.

To model the squaraine thin films, each system is treated as a dimer pair consisting of the nearest-neighbor  $\pi$ -stacked molecules along the crystalline  $a$  axis. The geometry of the dimer system is taken directly from the crystal structure.<sup>11,35,36</sup> Polarized and unpolarized absorbance spectra are calculated by assuming that the incident light is normal to the  $(0\ 0\ 1)$  crystal plane. A polarization angle of 0° corresponds to a polarization vector that is parallel to the projection of the long molecular axis onto the  $(0\ 0\ 1)$  plane. Increasing polarization angles correspond to the polarizer being rotated in a counterclockwise direction.

With the exception of the ion pair energy,  $\eta_{\text{CT}}$ , and the ICT integral,  $t_{\text{CT}}$ , all parameters are the same as in ref 35 (Table S2 in the Supporting Information). Both  $\eta_{\text{CT}}$  and  $t_{\text{CT}}$  are expected to depend on the packing geometry and are therefore allowed to vary between the systems studied. Specifically,  $\eta_{\text{CT}}$  and  $t_{\text{CT}}$  were optimized to reproduce the energy difference between the

two main absorption peaks,  $\Delta E = E_1 - E_2$ , and the ratio of their maximum intensity,  $R = I_1/I_2$ . The energy difference,  $\Delta E$ , is sensitive mainly to  $t_{CT}$ , and the peak ratio,  $R$ , is sensitive mainly to  $\eta_{CT}$ . The optimization was performed using the differential evolution algorithm in SciPy<sup>52</sup> with the objective of minimizing the sum of the squares of the residuals,  $(\Delta E_{\text{sim}} - \Delta E_{\text{exp}})^2 + (R_{\text{sim}} - R_{\text{exp}})^2$ . The remaining model parameters are all intramolecular parameters, and because the chromophore backbone is the same in all systems studied, they are not expected to vary significantly from system to system.

Although the dimer model is a simplification of the full three-dimensional crystalline system, it has been successfully used in previous studies to understand the main features of the absorbance spectra of *n*-alkyl anilino squarines,<sup>35,37</sup> and here it is also shown to account for the measured polarization dependence of the nHSQ and nOSQ spectra. A more sophisticated model might consider a larger number of molecules stacked along all three crystalline axes; however, this approach quickly becomes computationally intractable because the basis set grows exponentially with the number of molecules considered. In a recent study using an essential states model for dipolar molecules, Anzola and Painelli were able to study linear aggregates containing up to six molecules, but only after first exploiting translational symmetry and working in a rotated exciton basis that excluded states with large exciton numbers.<sup>53</sup> To the best of our knowledge, those are the largest systems that have been considered using an essential states model. Despite the limitations inherent to the dimer model, it still provides significant insight into the photophysics of *n*-alkyl anilino squaraines at a manageable computational cost.

## RESULTS AND DISCUSSION

**Unpolarized Absorbance of Extended Thin Films.** Figure 2 shows the absorbance spectra of spin-cast nBSQ, nPSQ, nHSQ, and nOSQ thin films. As documented previously,<sup>36</sup> the absorbance spectra of these thin films do not depend on polarization because they are polycrystalline and the size of the observation spot for the spectrometer is at least an order of magnitude larger than the size of the randomly distributed crystallites. The spectra of all four compounds show two characteristic humps with a short-wavelength (high-energy) and a long-wavelength (low-energy) maximum roughly peaking at  $\lambda \approx 550 \text{ nm} (\sim 2.25 \text{ eV})$  and  $\lambda \approx 650 \text{ nm} (\sim 1.91 \text{ eV})$ , respectively.

The essential states model was optimized to reproduce the difference in peak energy,  $\Delta E$ , and the peak height ratio,  $R$ , of the spin-cast samples for each compound by varying  $\eta_{CT}$  and  $t_{CT}$  (Table 1). Note that both  $t_{CT}$  and  $\eta_{CT}$  decrease with increasing alkyl chain length. The decrease in  $\eta_{CT}$  with increasing chain length contradicts the trend in this parameter for nBSQ and nHSQ in previous publications.<sup>35,37</sup> In those papers,  $\eta_{CT}$  increased from nBSQ to nHSQ, while here it decreased.

**Table 1. Optimized Modeling Parameters:  $\eta_{CT}^a$  and  $t_{CT}^b$**

parameter	nBSQ	nPSQ	nHSQ	nOSQ
$\eta_{CT}$ (eV)	1.4770	1.4700	1.4630	1.4540
$t_{CT}$ (eV)	0.3976	0.3395	0.3238	0.3116

<sup>a</sup>Mainly affects the peak ratio  $R$ . <sup>b</sup>Mainly affects the peak energy difference  $\Delta E$ .

These differences could arise from different methods used to determine optimal  $\eta_{CT}$  and  $t_{CT}$  or different experimental spectra used to fit the parameters. In any case, given the semiempirical nature of the model, the parameters should be considered to be effective values that may be compared between the different systems to establish trends. However, one must be careful when assigning meaning to the actual values. Furthermore, if we were able to consider larger systems, we would expect the optimum  $\eta_{CT}$  and  $t_{CT}$  to vary with the number of molecules in the system, eventually approaching converged values in the large system limit. However, the trends in  $\eta_{CT}$  and  $t_{CT}$  established using the dimer model are expected to be independent of system size.

The simulated spectra are compared to the experimental spectra in Figure 2. For all systems, the peak spacing,  $\Delta E$ , and ratio,  $R$ , of the simulated spectra are in good agreement with experiment. Especially the trend of decreasing  $t_{CT}$  and  $\eta_{CT}$  with increasing alkyl chain length clearly reproduces the relative increase of the short-wavelength peak and the narrowing of peak spacing, respectively, within the recorded spectra (Figure 2). The absolute peak energies,  $E$ , are in reasonable agreement with experiment, but the simulated spectra have slightly higher peak energies in all cases. Other disagreements between the simulations and experiments include the peak broadening. In the simulated spectra, the high-energy peak appears to be slightly narrower than the low-energy peak, which is opposite of the behavior observed in the experimental spectra (Figure 8c in ref 36). Better agreement between simulation and experiment could also be reached by fitting the line-broadening parameter to reproduce the experimental line width and by shifting the absolute peak energies of the simulated spectra to match the experiment. These optimizations would account for effects beyond the dimer model, such as structural disorder. However, because these would require a more complicated fitting procedure and offer limited additional insight into the photophysics of interest, we choose to neglect them here.

**Polarized Absorbance and Reflection of Microcrystalline Aggregates.** To gain better insight into the polarization dependence of the absorbance spectra, thin films with well-ordered larger but isolated aggregates are advantageous. Here, such aggregates have been prepared by dip coating and drop casting. Large-scale optical microscope images are presented in Figures 3(a) and 4(a) and in the Supporting Information section, where such aggregates can be clearly observed. AFM images (Figure S4) demonstrate that the aggregates are several hundred nanometers tall and well isolated from each other. The single-crystalline domain sizes are considered to be of the same order of magnitude as the focused probe beam spot size. Different from the spin-cast thin films, where a macroscopic probe beam averages over subwavelength-sized rotationally random domains, quasi-single-crystalline domains are inspected in the case of the microcrystalline aggregates. This reduces the impact of possible structural disorder, justifying the dimer model all the more.

The polarization analysis primarily targets the relative polarization difference in the two characteristic spectral features, specifically, the relative difference in azimuthal polarization direction,  $\Delta\phi$ , of both peaks within the plane of the sample. The sample was eucentrically adjusted and rotated in steps of 5° while the linear polarizer was kept in a fixed position. The polarization analysis was conducted in two different ways: pixelwise analysis of a series of microscopy images taken in reflection mode and an analysis of local

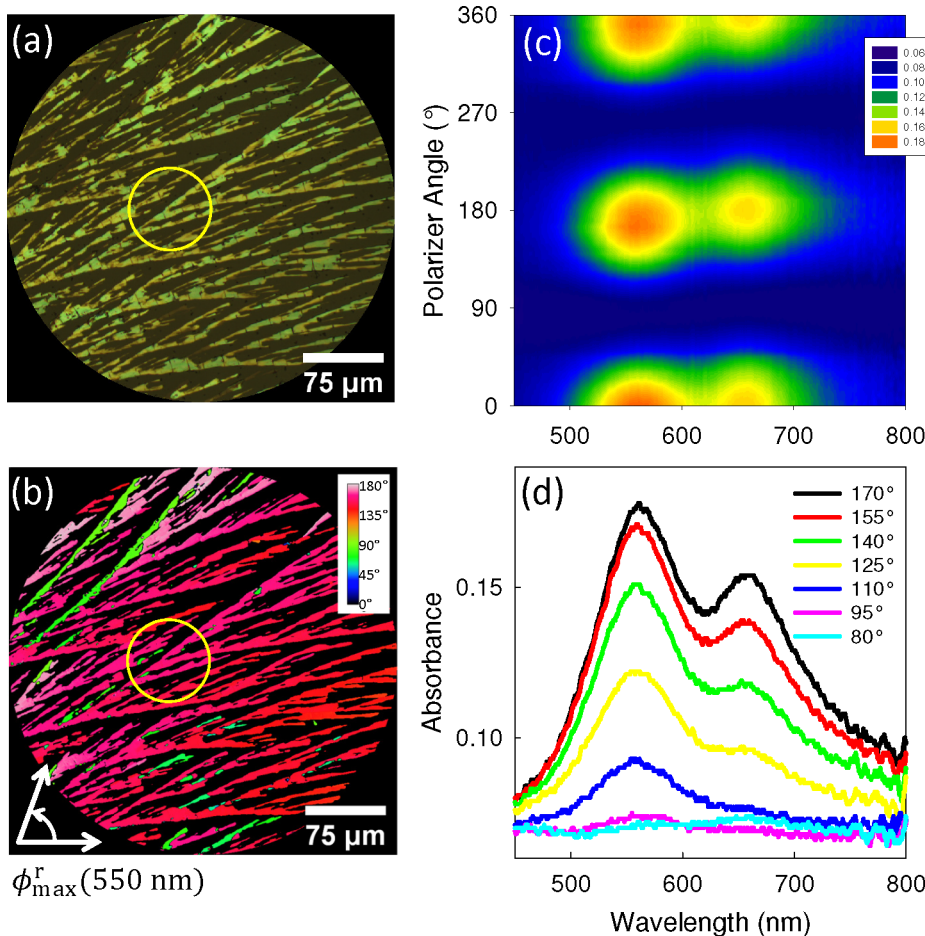


**Figure 3.** Polarized reflection and absorbance of nHSQ fibers on glass produced by dip coating. Single polarizer reflection microscope image (a) demonstrates the formation of fiber-like structures. Analyzing the reflectivity at 550 nm (b) shows that within the measurement area the angle for maximum reflectivity  $\phi_{\max}^r(550 \text{ nm})$  is well-defined; i.e., the in-plane orientation of the molecules is almost parallel. The coordinate system for the angle is sketched in the lower left. Polarized absorbance spectra, (c) and (d), depict the polarization angle dependence of the two absorption peaks. The yellow circle in (a) and (b) marks the area from where absorbance spectra have been taken. The single spectra in (d) cover a polarization angle range of 90° in steps of 15°, starting at the short-wavelength maximum. The difference in polarizer angle between the short- and long-wavelength maxima is  $\Delta\phi_{\max}^{\text{spec}} = (10 \pm 3)^\circ$ .

transmission spectra. This returns the azimuthal polarization direction in reflection  $\phi_{\max}^r$  and in transmission  $\phi_{\max}^t$  from image analysis and in transmission  $\phi_{\max}^{\text{spec}}$  from spectroscopic analysis and from this also the relative differences. For suitable fiber-like aggregates, the relative polarization angle between the long fiber axis and the polarization directions of each peak,  $\beta^t$ , is also determined from transmission image analysis.

For nHSQ, such a polarization analysis has been conducted for fiber-like aggregates close to the short- and long-wavelength absorption maxima at  $\lambda = 550 \text{ nm}$  (2.25 eV) and  $\lambda = 650 \text{ nm}$  (1.91 eV), respectively. The reflectivity is also peaking at these spectral positions, and the polarization angles are well-defined within microscopic regions. The angle for maximum reflectivity  $\phi_{\max}^r(550 \text{ nm})$  is shown in Figures 3(b) and S5(a), and the angle for maximum reflectivity  $\phi_{\max}^r(650 \text{ nm})$  can be found in Figure S5(b) (Supporting Information.) The difference  $\Delta\phi_{\max}^r = \phi_{\max}^r(650 \text{ nm}) - \phi_{\max}^r(550 \text{ nm})$  has been calculated from the images as shown in Figure S5(c) together with the corresponding histogram in Figure S5(d). This statistical analysis provides a positive and a negative maximum number, both having a value of  $|\Delta\phi_{\max}^r| = (7 \pm 3)^\circ$ . The reason for both a positive and a negative polarization angle difference is two aggregates with mirrored contact planes that are  $(0\ 0\ 1)$  and  $(0\$

$\bar{1}\ 0\ 0)$  (summarized as equivalent planes  $\{0\ 0\ 1\}$ ). For the chosen sample, a negative  $\Delta\phi_{\max}^r$  is more frequent (Figure S5(c)), and the respective fiber-like aggregates are color-coded red in Figure 3(b). An analysis for more fiber-like nHSQ aggregates (Figures S6 and S7) leads to similar results (see below). Adding a second crossed polarizer to the illumination arm and detecting the polarizer angle for light extinction at the two reflection maxima lead to comparable results, confirming their significance. This bireflection analysis is shown in the Supporting Information in Figure S5(e,f).

The difference in polarization angle has also been determined from polarized transmission spectra obtained from the nHSQ sample section marked by a yellow circle in Figure 3(a,b). From the transmission, the absorbance  $= -\log(T)$  is calculated, which is plotted in Figure 3(c,d). The contour plot in (c) contains all spectra for a full turn of the linear polarizer, and (d) shows only selected spectra covering an angular range of 90° in steps of 15°, starting at the short-wavelength maximum. The difference in polarization angle of the transmission spectroscopy maxima  $\Delta\phi_{\max}^{\text{spec}} = \phi_{\max}^{\text{spec}}(650 \text{ nm}) - \phi_{\max}^{\text{spec}}(550 \text{ nm})$  amounts to a slightly larger value of  $\Delta\phi_{\max}^{\text{spec}} = 10 \pm 3^\circ$ .

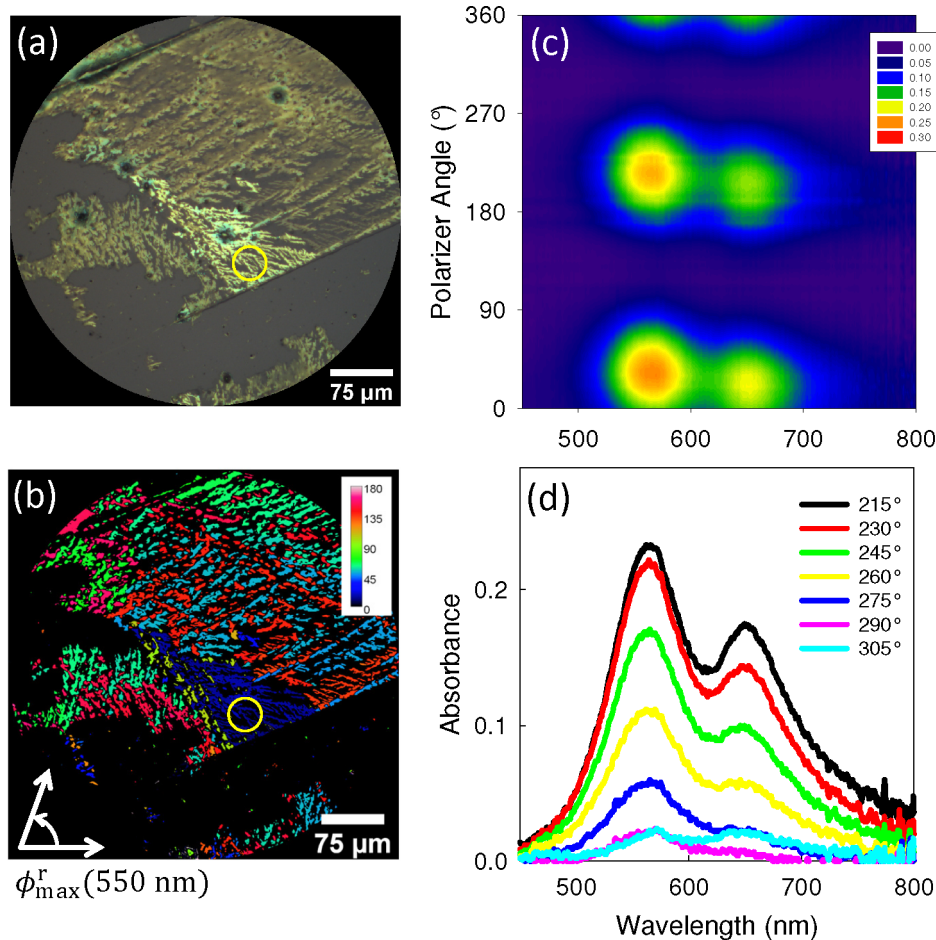


**Figure 4.** Same as Figure 3, but for nOSQ aggregates produced by dipcoating. Note that for the selected nOSQ sample section for spectroscopy as indicated by the yellow circle in (a) and (b) the larger wavelength maximum appears at a smaller polarizer angle than the short-wavelength maximum, opposite to the case of nHSQ. This time, for nOSQ the difference in polarizer angle between the short- and long-wavelength maximum obtained from transmission spectroscopy is  $|\Delta\phi_{\max}^{\text{spec}}| = (11 \pm 3)^\circ$ .

To make sure this discrepancy between  $\Delta\phi_{\max}^r$  and  $\Delta\phi_{\max}^{\text{spec}}$  is significant and not processing- and morphology-related, the polarization analysis has been repeated. This time, fiber-like nHSQ aggregates obtained from drop casting have been investigated by single polarizer reflection and transmission imaging (Supporting Information Figure S8) and not by spectroscopic means. The difference in polarizer angle for the reflection measurement was reproduced, being  $|\Delta\phi_{\max}^r| = (7 \pm 3)^\circ$  also for the drop-cast fiber-like nHSQ aggregates. Similarly, the difference in polarizer angle was found to be slightly larger for the transmission measurement, amounting to  $|\Delta\phi_{\max}^t| = (9 \pm 3)^\circ$ .

With that, the discrepancy between reflection and transmission analysis must be for a principal reason, which is related to the nature of the crystallographic system and the amount of polarization rotation on its way through the sample. Whereas for orthorhombic systems the principal axes of both the index ellipsoid and the absorption ellipsoid have to agree with the crystal axes,<sup>54–56</sup> this is not the case for triclinic crystals.<sup>57,58</sup> Triclinic unit cells are nonorthogonal systems, and the index and absorption ellipsoids are always orthogonal systems. With that, their orientation is even wavelength-dependent (axial dispersion).<sup>59,60</sup> This also means that the polarizer angles for maxima and minima are in reflected and transmitted intensity, respectively. Even under normal incidence they are not

necessarily congruent for triclinic crystals. For nHSQ and nOSQ the index ellipsoid and the absorbance ellipsoid are essentially not known up to now. However, we estimate their orientational deviation from each other to be small since the inspected aggregate thickness is well below 1  $\mu\text{m}$ .

The same type of analysis has been performed on nOSQ microcrystallites obtained from dip coating (Figure 4). The nOSQ did not grow into such distinct fiber-like aggregates but rather showed fractal-like microaggregates with extended areas of homogeneous polarization. Here, the difference angle in transmission for the two absorbance maxima determined by spectroscopy is  $|\Delta\phi_{\max}^{\text{spec}}| = (11 \pm 3)^\circ$ . Note that for the selected nOSQ sample section as indicated by the yellow circle in Figure 4(a,b) the larger wavelength maximum appears at a smaller polarizer angle than the short-wavelength maximum, opposite to the case of nHSQ. Also for nOSQ the two mirror-image but otherwise equivalent crystallographic orientations ( $(0\ 0\ \bar{1})$  and  $(0\ 0\ 1)$ ) are realized. The polarization analysis from imaging in transmission and reflection of the nOSQ sample is shown in the Supporting Information in Figure S8. From the histograms in Figure S8(c,d), values of  $|\Delta\phi_{\max}^t| = (12 \pm 3)^\circ$  and  $|\Delta\phi_{\max}^r| = (8 \pm 3)^\circ$  have been determined, respectively. Again, the value for the difference in polarization angle is consistently larger for the transmission analysis of nOSQ for the reason of adopting a low-symmetry triclinic crystallo-

graphic unit cell.<sup>57–60</sup> In Table 2, the experimentally determined values of all  $\Delta\phi$  for nHSQ and nOSQ are

**Table 2.** Difference in Polarization Angle  $\Delta\phi$  Obtained from Reflection and Transmission Images and Spectroscopic Transmission Analysis as Well as Their Average Values

compound	$ \Delta\phi_{\max}^r $ (deg)	$ \Delta\phi_{\max}^t $ (deg)	$ \Delta\phi_{\max}^{\text{spec}} $ (deg)	$ \Delta\phi_{\max}^{\text{ave}} $ (deg)
nHSQ	$7 \pm 3$	$9 \pm 3$	$10 \pm 3$	$9 \pm 5$
nOSQ	$8 \pm 3$	$12 \pm 3$	$11 \pm 3$	$10 \pm 5$

summarized together with their calculated average. The respective average value  $|\phi_{\max}^{\text{ave}}|$  is used in the following section for comparison with the simulated data.

**Origin of Polarization Dependence: Modeling.** Polarized absorbance spectra were simulated using the parameters in Table 1 and Supporting Information Table S2. In all cases, the incident light is normal to the (0 0 1) crystal face. A polarization angle of  $0^\circ$  corresponds to a polarization vector that is parallel to the projection of the long molecular axis onto the (0 0 1) plane. As the polarization angle increases from  $0^\circ$ , the polarizer is rotated in a counterclockwise direction (Figure 5).

Contour plots of the absorbance spectra as a function of polarizer angle are shown in Figure 6. For nHSQ and nOSQ, these can be compared to the experimental measurements shown in Figures 3 and 4. The experimentally measured polarization dependence is reproduced well by the simulations. In particular, the low- and high-energy peaks in the simulated spectra show maxima at polarization angles separated by about  $|\Delta\phi| = 13^\circ$  and  $12^\circ$  for nHSQ and nOSQ, respectively (Table 3). This is in good agreement with the experimental

measurements for nHSQ and nOSQ, for which the peaks have maxima at angular differences of about  $|\Delta\phi_{\max}^{\text{ave}}| \approx 10^\circ$ .

The polarization dependence arises from the different orientations of the molecular and charge-transfer transition dipole moments and their relative contribution to the total transition dipole moment of the absorbing states. The molecular transition dipole is oriented along the long axis of the molecule, and the charge-transfer transition dipole is oriented along the  $\pi$ -stacking axis; see below. When the transition dipole moment of the absorbing state is dominated by a large molecular transition dipole component, absorbance is polarized mostly along the long molecular axis. In contrast, when the transition dipole moment is dominated by a large charge-transfer transition dipole component, absorbance is polarized mostly along the  $\pi$ -stacking axis. By varying the molecular versus charge-transfer composition of the transition dipole moment, the absorption polarization varies between these two extremes.

To understand the origin of the polarization dependence, the transition dipole moment for each excited state was decomposed into its molecular (M) and charge-transfer (CT) components,  $\mu_M$  and  $\mu_{\text{CT}}$ , respectively. See the Supporting Information for calculation details. Table 4 shows the molecular and charge-transfer components of the transition dipole moments for the states contributing the largest oscillator strength to each absorption peak.

For each state shown in Table 4, the charge-transfer component,  $|\mu_{\text{CT}}|$ , is only about 10–20% as large as the molecular component,  $|\mu_M|$ . The large difference in magnitude between  $|\mu_{\text{CT}}|$  and  $|\mu_M|$  is the origin of the observed polarization dependence in Figure 6.

As discussed in ref 35, the electronic states responsible for the absorbance spectra of squaraine thin films can be adequately described as a linear combination of the neutral

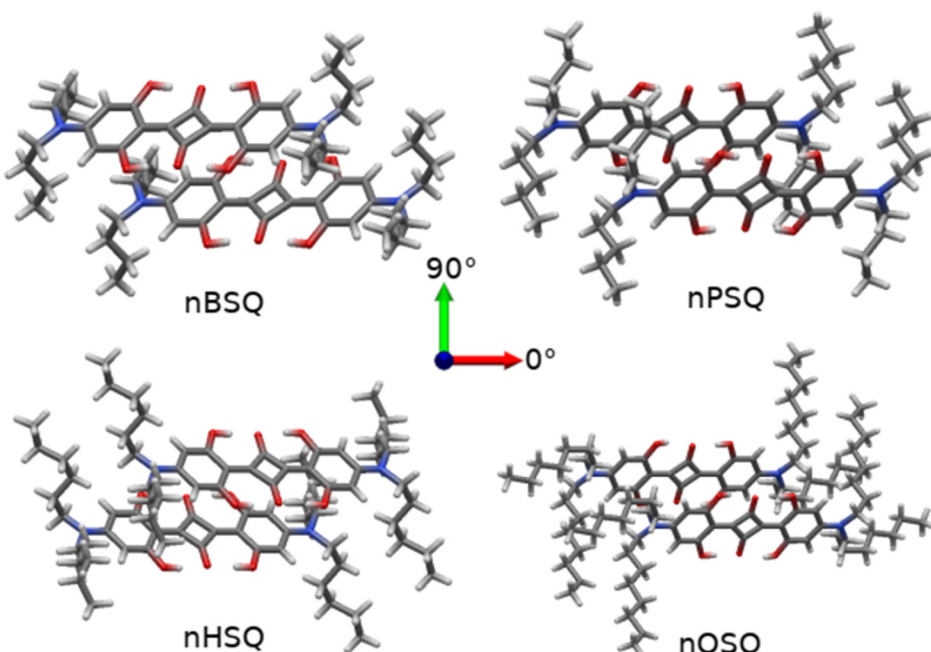


**Figure 5.** Dimer geometries in the orthogonal laboratory reference frame extracted from the single-crystal structure data. Incident light travels along the  $-z$  laboratory axis. Light is polarized at  $0^\circ$  when the polarization vector is parallel to the laboratory  $x$  axis (red axis). The polarization angle increases in the counterclockwise direction so that light is polarized at  $90^\circ$  when the polarization vector is parallel to the laboratory  $y$  axis (green axis). Note that for nHSQ the molecules  $\pi$ -stack "up and to the right" while for the other systems the molecules stack "up and to the left".

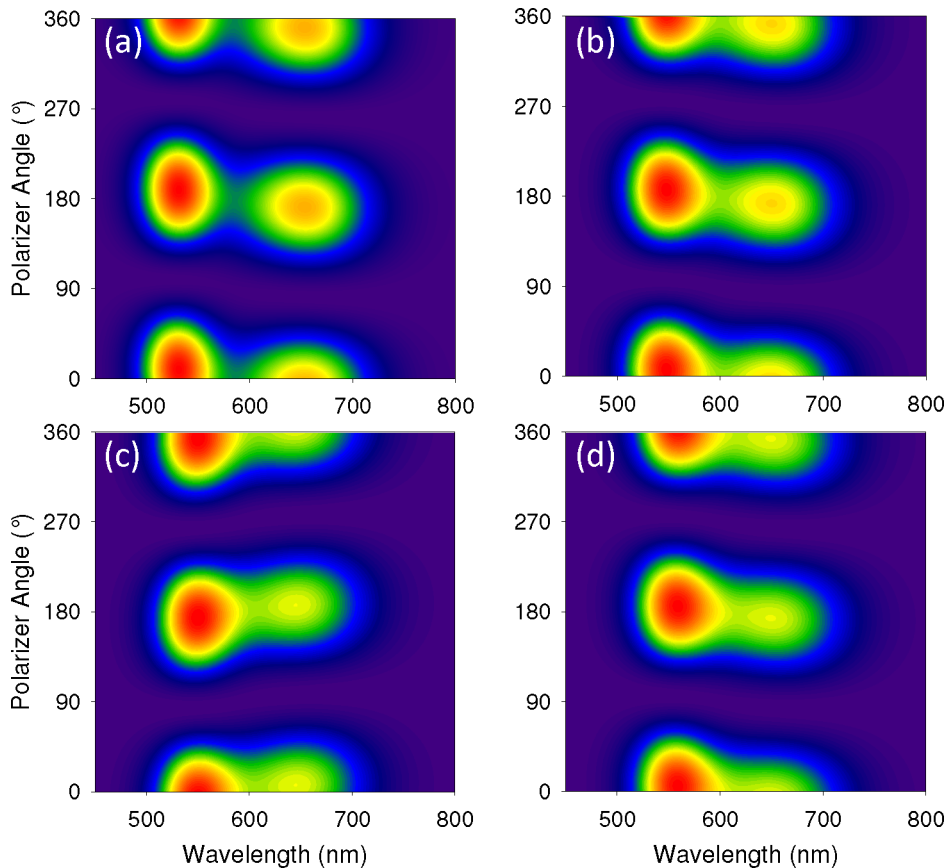


**Figure 6.** Simulated absorbance spectra for (a) nBSQ, (b) nPSQ, (c) nHSQ, and (d) nOSQ as a function of polarizer angle. Dark blue indicates regions of low absorbance, and red indicates regions of high absorbance. Note that for nHSQ the simulations predict that the short-wavelength peak has a maximum at a smaller polarization angle than for the long-wavelength peak. This is a result of the different stacking geometry (Figure 5), resulting in the CT dipole “pointing” in a different direction for nHSQ than for the other systems. The simulations show the same behavior as in the experiments (Figures 3 and 4).

**Table 3. Polarizer Angle of Maximum Intensity for the High (Peak 1) and Low (Peak 2) Energy Peaks for the Simulated Spectra<sup>a</sup>**

species	peak 1 (deg)	peak 2 (deg)	calcd $\Delta\phi$ (deg)	$\Delta\phi_{\max}^{\text{ave}}$ (deg)
nBSQ	189	172	17	
nPSQ	187	173	14	
nHSQ	174	187	13	$9 \pm 5$
nOSQ	186	174	12	$10 \pm 5$

<sup>a</sup>The angle difference  $\Delta\phi$  between maxima is also reported. The experimentally determined value is the average over transmission and reflection measurements  $|\Delta\phi_{\max}^{\text{ave}}|$ , as also given in Table 2.

**Table 4. Total  $|\mu^{k=0}|$ , Molecular  $|\mu_M^{k=0}|$ , and Charge-Transfer  $|\mu_{CT}^{k=0}|$  Ground to the  $k$ th Excited State Transition Dipole Moments for the Excited States of nBSQ, nPSQ, nHSQ, and nOSQ<sup>a</sup>**

system	state ( $k$ )	energy (eV)	$ \mu^{k=0} $ (D)	$ \mu_M^{k=0} $ (D)	$ \mu_{CT}^{k=0} $ (D)
nBSQ	105	1.8542	14.1	13.4	2.5
	165	2.3455	11.5	11.0	1.9
nPSQ	108	1.8501	13.7	13.1	2.2
	162	2.2818	15.2	14.7	2.1
nHSQ	108	1.8542	13.1	12.7	2.1
	161	2.2731	15.6	15.1	2.0
nOSQ	107	1.8341	12.9	12.3	2.1
	161	2.2418	15.5	15.1	1.9

<sup>a</sup>Only the two states with the largest oscillator strengths are shown. Other states also contribute to the absorbance spectra. The values have been rounded to one decimal place.

and charge-separated states  $|ge_1\rangle_{AS}$  and  $|ac_1\rangle_{AS}$ . The state  $|ge_1\rangle_{AS}$  is the optically allowed intramolecular exciton, and  $|ac_1\rangle_{AS}$  is the lowest-energy antisymmetric ICT state. In the absence of intermolecular interactions and vibronic coupling,  $|ge_1\rangle_{AS}$  and  $|ac_1\rangle_{AS}$  are eigenstates of the system and  $|ge_1\rangle_{AS}$  is the only state with a nonzero transition dipole moment,  $\mu_M^{(0)}$ , from the symmetric ground state  $|gg\rangle_S$  (Figure 7(a)). In the absence of charge-transfer interactions,  $|gg\rangle_S$  has zero charge-transfer character and absorbance to charge-transfer states such as  $|ac_1\rangle_{AS}$  is forbidden. Once the intermolecular charge-transfer interactions are turned on, however, two important changes occur in the ground- and excited-state wave functions. First,  $|gg\rangle_S$  mixes with higher-lying charge-transfer states to form a new ground state  $|IG\rangle_S$  of mixed neutral and charge-transfer

character (Figure 7(b)). The new ground state results in new transition dipole moments from the ground state to  $|ge_1\rangle_{AS}$  and  $|ac_1\rangle_{AS}$ , namely,  $\mu_M^{(1)}$  and  $\mu_{CT}^{(1)}$ . Importantly, the transition to  $|ac_1\rangle_{AS}$  is no longer forbidden because the charge-transfer character of  $|IG\rangle_S$  gives rise to a nonzero charge-transfer transition dipole moment  $\mu_{CT}^{(1)}$ . For the parameters relevant to the squaraine systems studied here, the charge-transfer admixture to  $|IG\rangle_S$  is small, which restricts  $\mu_{CT}^{(1)}$  to be a small fraction of  $\mu_M^{(1)}$  (Table S3 in the Supporting Information).

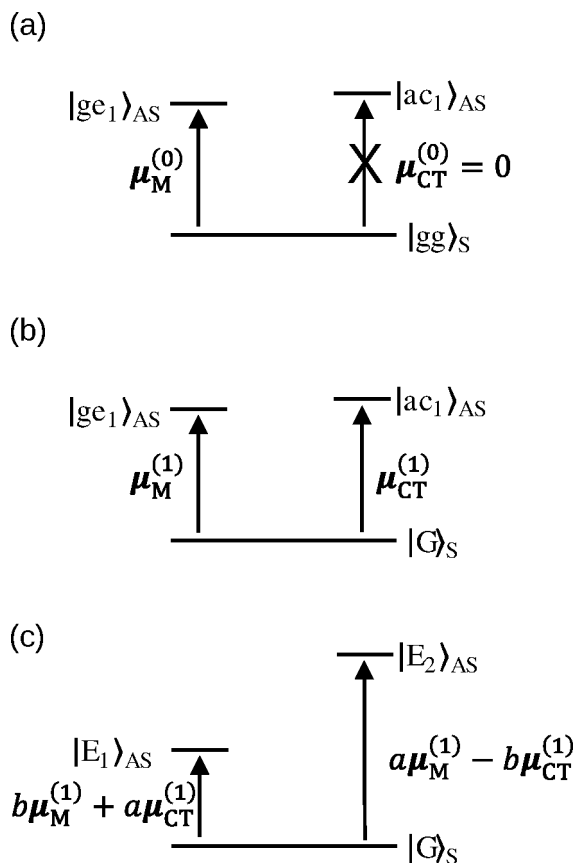


**Figure 7.** Energy-level diagrams showing the electronic states relevant to the absorption processes in the squaraine systems considered here. (a) In the absence of intermolecular interactions and vibronic coupling, the ground state,  $|gg\rangle_S$ , has zero charge-transfer character, and only one excited state,  $|ge_1\rangle_{AS}$ , has a finite transition dipole moment,  $\mu_M^{(0)}$ . All other states, including  $|ac_1\rangle_{AS}$ , which is nearly resonant with  $|ge_1\rangle_{AS}$ , are dark. (b) When intermolecular charge-transfer interactions are turned on, the ground state,  $|gg\rangle_S$ , mixes with higher-lying charge-transfer states (not shown) to form a new ground state,  $|G\rangle_S$ , with charge-transfer character and a finite transition dipole to  $|ac_1\rangle_{AS}$ ,  $\mu_{CT}^{(1)}$ . The new ground state also modifies the transition dipole to  $|ge_1\rangle_{AS}$  to  $\mu_M^{(1)}$ . (c) Intermolecular charge-transfer interactions cause mixing between  $|ge_1\rangle_{AS}$  and  $|ac_1\rangle_{AS}$  to create two new excited states  $|E_1\rangle_{AS} \approx b|ge_1\rangle_{AS} + a|ac_1\rangle_{AS}$  and  $|E_2\rangle_{AS} \approx a|ge_1\rangle_{AS} - b|ac_1\rangle_{AS}$ , where  $a$  and  $b$  are the mixing coefficients. The transition dipole moments to these states are linear combinations of  $\mu_M^{(1)}$  and  $\mu_{CT}^{(1)}$  weighted by coefficients  $a$  and  $b$ .

The second important development that occurs when the charge-transfer interactions are turned on is the mixing of  $|ge_1\rangle_{AS}$  and  $|ac_1\rangle_{AS}$  to form new excited states  $|E_1\rangle_{AS} \approx b|ge_1\rangle_{AS} + a|ac_1\rangle_{AS}$  and  $|E_2\rangle_{AS} \approx a|ge_1\rangle_{AS} - b|ac_1\rangle_{AS}$ , where  $a$  and  $b$  are the mixing coefficients (Figure 7(c)). (We note that other higher-energy states mix into  $|E_1\rangle_{AS}$  and  $|E_2\rangle_{AS}$  to a smaller degree, but we omit the details for the sake of clarity.) For the parameters relevant to the squaraine systems studied here,  $|ge_1\rangle_{AS}$  and  $|ac_1\rangle_{AS}$  are nearly resonant so that  $a$  and  $b$  are of comparable magnitude. The transition dipole moments to the new excited states are linear combinations of  $\mu_M^{(1)}$  and  $\mu_{CT}^{(1)}$  weighted by the coefficients  $a$  and  $b$ . For  $|E_1\rangle_{AS}$ , the dipole moment is approximately  $b\mu_M^{(1)} + a\mu_{CT}^{(1)}$ , and for  $|E_2\rangle_{AS}$ , the dipole moment is approximately  $a\mu_M^{(1)} - b\mu_{CT}^{(1)}$  (Figure 7(c)). Because  $\mu_M^{(1)}$  and  $\mu_{CT}^{(1)}$  have different orientations, absorbances to  $|E_1\rangle_{AS}$  and  $|E_2\rangle_{AS}$  are polarized differently. However, because

the magnitude of  $\mu_{CT}^{(1)}$  is small compared to that of  $\mu_M^{(1)}$  and  $a$  and  $b$  are of comparable magnitude, the difference in polarization angle between  $|E_1\rangle_{AS}$  and  $|E_2\rangle_{AS}$  is relatively small.

This behavior is demonstrated for the relevant states of the full simulations in Table 5, which shows the  $x$  and  $y$

**Table 5.**  $x$  and  $y$  Components of the Molecular and Charge-Transfer Transition Dipole Moments in the Laboratory Reference Frame for Each State Listed in Table 4<sup>a</sup>

system	state ( $k$ )	$\mu_x^{k=0}$ (D)	$\mu_y^{k=0}$ (D)	$\mu_{M,x}^{k=0}$ (D)	$\mu_{M,y}^{k=0}$ (D)	$\mu_{CT,x}^{k=0}$ (D)	$\mu_{CT,y}^{k=0}$ (D)
nBSQ	105	-13.0	2.2	-12.2	0.0	-0.8	2.2
	165	10.1	1.7	10.0	0.0	0.1	1.7
nPSQ	108	12.8	-1.9	12.1	0.0	0.7	-1.9
	162	13.4	1.9	13.5	0.0	0.0	1.9
nHSQ	108	12.1	1.8	11.5	0.0	0.6	1.8
	161	-13.8	1.7	-13.7	0.0	0.0	1.7
nOSQ	107	12.0	-1.8	11.3	0.0	0.7	-1.8
	161	13.8	1.7	13.9	0.0	-0.1	1.7

<sup>a</sup>The values have been rounded to one decimal place. See Figure 5 for the definition of the laboratory reference frame.

components of the total, molecular, and charge-transfer dipole moments of the excited states in the laboratory reference frame. Because the CT component is small compared to the molecular component, the direction of the total transition dipole moment is determined mainly by the direction of the molecular component, hence the relatively small difference between the polarization angle of maximum intensity for the two absorption peaks.

A qualitative picture of this polarization behavior is shown for nHSQ in Figure 8. Note that simple graphical vector addition of the lilac and cyan arrows indicating the molecular and CT transition dipole moments based on the projected structural parameters would not work. This approximation is valid only for excitons composed of transition dipole moments with equal oscillator strengths and prevailing Coulombic interactions.<sup>30,31</sup>

For nHSQ, fiber-like aggregates have been found (Figure 3 and Figures S6 and S7). Therefore, angle  $\beta^t$  of the polarized absorbance maximum with respect to the long fiber axis is well-defined. The experimentally found angle  $\beta_{550}^t$  at the short-wavelength maximum is found to be  $\pm 44 \pm 3$  and  $\pm 45 \pm 3^\circ$  for the nHSQ samples presented in Figures 3 and S7, respectively. For the angle at the long-wavelength maximum,  $\beta_{650}^t$ , two mirror-image main values have been found for the two samples. These are  $90 - (53 \pm 3) = (37 \pm 3)$  and  $(36 \pm 3)^\circ$ , respectively. Now considering that the growth direction of the long fiber axis is the molecular stacking direction, the crystallographic  $a$ -axis or the [1 0 0] direction runs along the long nHSQ fiber axis. This is indicated by a broad light-green arrow in Figure 8(a) overlaid on two nearest-neighbor molecules and the crystallographic unit cell with the (0 0 1) orientation. The lilac and cyan arrows indicate the directions of the molecular and CT transition dipole moments, respectively, based on the sketched structural parameters, but because the CT transition dipole moment is comparatively small, the net transition dipole moments (black arrows) are largely determined by the molecular transition dipole moment (Figure 8(b)). With an angle of approximately  $|\Delta\phi| = 10^\circ$  in between these measurable excitonic net transition dipole moments, their projected angles onto the (0 0 1) plane with respect to the

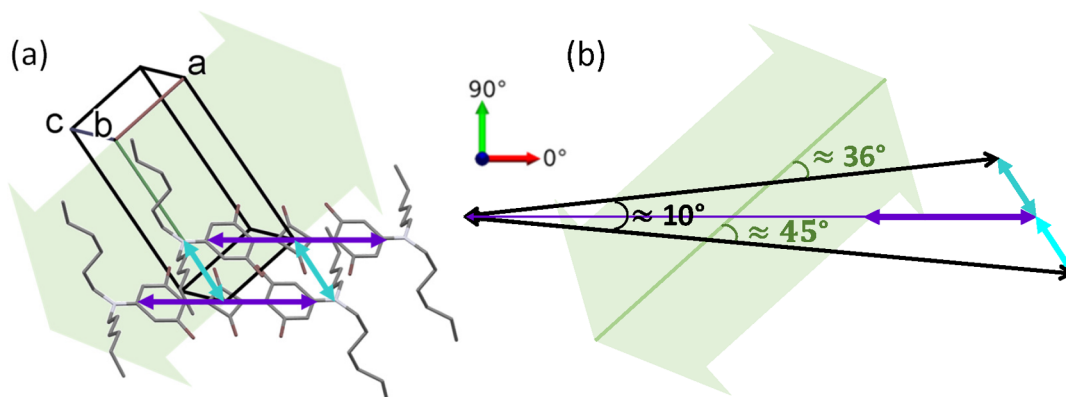


**Figure 8.** (a) Qualitative picture of the molecular (lilac) and intermolecular charge-transfer (cyan) transition dipole moments for nHSQ, overlaid on the dimer in the orthogonal laboratory reference frame (red arrow  $0^\circ$ , green arrow  $90^\circ$ ). The corresponding crystallographic unit cell projected onto the  $(0\ 0\ 1)$  plane is also shown. The broad light-green arrow points out the possible direction of the long fiber-like aggregate axis, that is, the crystallographic  $a$  axis or  $[1\ 0\ 0]$ . (b) Black arrows represent a qualitative picture of the sum and difference of the molecular (lilac) and CT transition (cyan) dipole moments. Because the CT transition dipole moment is relatively small compared to the molecular transition dipole moment, the directions of the net dipoles are largely determined by the molecular transition dipole moment. There is a relatively small angle (approximately  $|\Delta\phi| = 10^\circ$ ) between the two measurable net transition dipole vectors (black arrows). These two net transition dipole moments have angles of about 36 and  $45^\circ$ , respectively, with the possible long fiber-like aggregate axis (broad light-green arrow) being along the crystallographic  $a$  axis.

long fiber axis (crystallographic  $a$  axis) are about 36 and  $45^\circ$ , respectively (Figure 8(b)). Indeed, this is observed by the experimental polarization analysis of the  $\beta^t$  angles supporting the picture of molecular orientation within the nHSQ fiber-like aggregates.

## CONCLUSIONS

We have affirmed a previously established essential state model for the formation of hybrid intermolecular charge-transfer and intramolecular Frenkel excitons for *n*-alkyl-terminated anilino squaraines in well-ordered microcrystalline-textured thin films. The newly determined crystal structure of nOSQ (*n*-octyl) extends the known series of nBSQ (*n*-butyl), nPSQ (*n*-pentyl), and nHSQ (*n*-hexyl) and allows us to point out clear trends for the intermolecular charge-transfer integral  $t_{CT}$  and the ion pair energy  $\eta_{CT}$ : both parameters decrease with increasing alkyl chain length. This is expressed in the absorbance spectra by a relative increase in the short-wavelength spectral feature and a decrease in the peak energy difference of both spectral features. These generic double-hump spectral signatures exhibit characteristic linear dichroism with a relatively small angle between the two net transition dipole moment vectors, which cannot be understood by spatial considerations based on the crystallographic data of the triclinic unit cell. The key to resolving the spatial polarization pattern with respect to the micromorphology is to account for the different contribution strengths of the molecular and charge-transfer transition dipole moments. Essential states modeling finds that the charge-transfer transition dipole moment is small compared to the molecular transition dipole moment so that the directions of the measurable net transition dipole moments are largely determined by the molecular component. This illustrates the power of spatially and polarization-resolved analysis combined with theoretical considerations to obtain a deeper understanding of excited states in microtextured thin films.

## ASSOCIATED CONTENT

### Supporting Information

The Supporting Information is available free of charge at <https://pubs.acs.org/doi/10.1021/acs.jpcc.2c03665>.

Plots of the crystal structures of nBSQ, nPSQ, nHSQ, and nOSQ; unpolarized absorbance spectra together with reflection microscopy and AFM images of nHSQ and nOSQ thin films; AFM images of nHSQ and nOSQ fibers; additional details on the modeling of optical spectra by the extended essential states model; and additional details on the polarization analysis of nHSQ and nOSQ fibrous aggregates (PDF)

## AUTHOR INFORMATION

### Corresponding Author

Manuela Schiek – Institute of Physical Chemistry and Linz Institute for Organic Solar Cells (LIOS) & Center for Nano-Analytics (ZONA), Johannes Kepler University, A-4040 Linz, Austria; [orcid.org/0000-0002-0108-2998](https://orcid.org/0000-0002-0108-2998); Email: [manuela.schiek@jku.at](mailto:manuela.schiek@jku.at)

### Authors

Frank Balzer – SDU Centre for Photonics Engineering, University of Southern Denmark, DK-6400 Sønderborg, Denmark; [orcid.org/0000-0002-6228-6839](https://orcid.org/0000-0002-6228-6839)

Nicholas J. Hestand – Department of Natural and Applied Sciences, Evangel University, Springfield, Missouri 65802, United States; [orcid.org/0000-0001-7522-2466](https://orcid.org/0000-0001-7522-2466)

Jennifer Zablocki – Kekulé-Institute for Organic Chemistry and Biochemistry, University of Bonn, D-53121 Bonn, Germany; [orcid.org/0000-0002-2100-4807](https://orcid.org/0000-0002-2100-4807)

Gregor Schnakenburg – Institute of Inorganic Chemistry, University of Bonn, D-53121 Bonn, Germany; [orcid.org/0000-0001-6489-2106](https://orcid.org/0000-0001-6489-2106)

Arne Lützen – Kekulé-Institute for Organic Chemistry and Biochemistry, University of Bonn, D-53121 Bonn, Germany; [orcid.org/0000-0003-4429-0823](https://orcid.org/0000-0003-4429-0823)

Complete contact information is available at:

<https://pubs.acs.org/10.1021/acs.jpcc.2c03665>

## Notes

The authors declare no competing financial interest.

## ACKNOWLEDGMENTS

M. S. thanks the PRO RETINA foundation (especially Franz Badura) and the Linz Institute of Technology (LIT-2019-7-INC-313 SEAMBIOF) for funding. J. Z. and A. L. gratefully acknowledge financial support from the DFG (RTG 2591 Template-designed Organic Electronics).

## REFERENCES

- (1) He, J.; Jo, Y. J.; Sun, X.; Qiao, W.; Ok, J.; Kim, T.; Li, Z. Squaraine Dyes for Photovoltaic and Biomedical Applications. *Adv. Funct. Mater.* **2021**, *31*, 2008201.
- (2) Gsänger, M.; Bialas, D.; Huang, L.; Stolte, M.; Würthner, F. Organic Semiconductors based on Dyes and Color Pigments. *Adv. Mater.* **2016**, *28*, 3615–3645.
- (3) Halton, B. From Small Rings to Big Things: Xerography, Sensors, and the Squaraines. *Chem. New Zealand* **2008**, *72*, 57–62.
- (4) Beverina, L.; Salice, P. Squaraine Compounds: Tailored Design and Synthesis towards a Variety of Material Science Applications. *Eur. J. Org. Chem.* **2010**, *2010*, 1207–1225.
- (5) Weiss, D. S. The History and Development of Organic Photoconductors for Electrophotography. *J. Imaging Sci. Technol.* **2016**, *60*, 30505-1–30505-24.
- (6) Law, K.-Y. Organic Photoconductive Materials: Recent Trends and Developments. *Chem. Rev.* **1993**, *93*, 449–486.
- (7) Chen, Y.; Zhu, W.; Wu, J.; Huang, Y.; Fachetti, A.; Marks, T. J. Recent Advances in Squaraine Dyes for Bulk-Heterojunction Organic Solar Cells. *Org. Photonics Photovolta.* **2019**, *6*, 1–16.
- (8) Maeda, T.; Nguyen, T. V.; Kuwano, Y.; Chen, X.; Miyanaga, K.; Nakazumi, H.; Yagi, S.; Soman, S.; Ajayaghosh, A. Intramolecular Exciton-Coupled Squaraine Dyes for Dye-Sensitized Solar Cells. *J. Phys. Chem. C* **2018**, *122*, 21745–21754.
- (9) Chen, G.; Sasabe, H.; Lu, W.; Wang, X.-F.; Kido, J.; Hong, Z.; Yang, Y. J-aggregation of a squaraine dye and its application in organic photovoltaic cells. *J. Mater. Chem. C* **2013**, *1*, 6547–6552.
- (10) Deing, K. C.; Mayerhöffer, U.; Würthner, F.; Meerholz, K. Aggregation-dependent photovoltaic properties of squaraine/PC<sub>61</sub>BM bulk heterojunctions. *Phys. Chem. Chem. Phys.* **2012**, *14*, 8328.
- (11) Brück, S.; Krause, C.; Turrisi, R.; Beverina, L.; Wilken, S.; Saak, W.; Lützen, A.; Borchert, H.; Schiek, M.; Parisi, J. Structure-property relationship of anilino-squaraines in organic solar cells. *Phys. Chem. Chem. Phys.* **2014**, *16*, 1067–1077.
- (12) Somashekharappa, G. M.; Govind, C.; Pulikodan, V.; Paul, M.; Namboothiry, M. A. G.; Das, S.; Karunakaran, V. Unsymmetrical Squaraine Dye-Based Organic Photodetector Exhibiting Enhanced Near-Infrared Sensitivity. *J. Phys. Chem. C* **2020**, *124*, 21730–21739.
- (13) Schulz, M.; Balzer, F.; Scheunemann, D.; Arteaga, O.; Lützen, A.; Meskers, S.; Schiek, M. Chiral Excitonic Organic Photodiodes for Direct Detection of Circular Polarized Light. *Adv. Funct. Mater.* **2019**, *29*, 1900684.
- (14) Strassel, K.; Kaiser, A.; Jenatsch, S.; Véron, A. C.; Anantharaman, S. B.; Hack, E.; Diethelm, M.; Nüesch, F.; Aderne, R.; Legnani, C.; et al. Squaraine Dye for a Visibly Transparent All-Organic Optical Upconversion Device with Sensitivity at 1000 nm. *ACS Appl. Mater. Interfaces* **2018**, *10*, 11063–11069.
- (15) Binda, M.; Iacchetti, A.; Natali, D.; Beverina, L.; Sassi, M.; Sampietro, M. High detectivity squaraine-based near infrared photodetector with nA/cm<sup>2</sup> dark current. *Appl. Phys. Lett.* **2011**, *98*, 073303.
- (16) Abdullaeva, O. S.; Balzer, F.; Schulz, M.; Parisi, J.; Lützen, A.; Dedek, K.; Schiek, M. Organic Photovoltaic Sensors for Photocapacitive Stimulation of Voltage-Gated Ion Channels in Neuroblastoma Cells. *Adv. Funct. Mater.* **2019**, *29*, 1805177.
- (17) Gsänger, M.; Kirchner, E.; Stolte, M.; Burschka, C.; Stepanenko, V.; Pflaum, J.; Würthner, F. High-Performance Organic Thin-Film Transistors of J-Stacked Squaraine Dyes. *J. Am. Chem. Soc.* **2014**, *136*, 2351–2362.
- (18) Avirah, R. R.; Jayaram, D. T.; Adarsh, N.; Ramaiah, D. Squaraine dyes in PDT: from basic design to in vivo demonstration. *Org. Biomol. Chem.* **2012**, *10*, 911–920.
- (19) Babu, P. S. S.; Manu, P. M.; Dhanya, T. J.; Tapas, P.; Meera, R. N.; Surendran, A.; Aneesh, K. A.; Vadakkancheril, S. J.; Ramaiah, D.; Nair, S. A.; et al. Bis(3,5-diiodo-2,4,6-trihydroxyphenyl)squareaine photodynamic therapy disrupts redox homeostasis and induce mitochondria-mediated apoptosis in human breast cancer cells. *Sci. Rep.* **2017**, *7*, 42126.
- (20) Sreejith, S.; Joseph, J.; Lin, M.; Menon, N. V.; Borah, P.; Ng, H. J.; Loong, Y. X.; Kang, Y.; Yu, S. W.-K.; Zhao, Y. Near-Infrared Squaraine Dye Encapsulated Micelles for in Vivo Fluorescence and Photoacoustic Bimodal Imaging. *ACS Nano* **2015**, *9*, 5695–5704.
- (21) Wu, D.; Chen, L.; Lee, W.; Ko, G.; Yin, J.; Yoon, J. Recent progress in the development of organic dye based near-infrared fluorescence probes for metal ions. *Coord. Chem. Rev.* **2018**, *354*, 74–97.
- (22) Saikin, S. K.; Eisfeld, A.; Valneau, S.; Aspuru-Guzik, A. Photonics meets excitonics: natural and artificial molecular aggregates. *Nanophotonics* **2013**, *2*, 21–38.
- (23) Painelli, A.; Terenziani, F. Along the way from molecules to devices. *Synth. Met.* **2004**, *147*, 111–115.
- (24) Rösch, A. T.; Zhu, Q.; Robben, J.; Tassinari, F.; Meskers, S. C. J.; Naaman, R.; Palmans, A. R. A.; Meijer, E. W. Helicity Control in the Aggregation of Achiral Squaraine Dyes in Solution and Thin Films. *Chem. - Eur. J.* **2021**, *27*, 298–306.
- (25) Shen, C.-A.; Bialas, D.; Hecht, M.; Stepanenko, V.; Sugiyasu, K.; Würthner, F. Polymorphism in Squaraine Dye Aggregates by Self-Assembly Pathway Differentiation: Panchromatic Tubular Dye Nanorods versus J-Aggregate Nanosheets. *Angew. Chem.* **2021**, *133*, 12056–12065.
- (26) Shen, C.-A.; Würthner, F. NIR-emitting squaraine J-aggregate nanosheets. *Chem. Commun.* **2020**, *56*, 9878–9881.
- (27) Röhr, M. I. S.; Marciak, H.; Hoche, J.; Schreck, M. H.; Ceymann, H.; Mitric, R.; Lambert, C. Exciton Dynamics from Strong to Weak Coupling Limit Illustrated on a Series of Squaraine Dimers. *J. Phys. Chem. C* **2018**, *122*, 8082–8093.
- (28) Bialas, D.; Kirchner, E.; Röhr, M. I. S.; Würthner, F. Perspectives in Dye Chemistry: A Rational Approach toward Functional Materials by Understanding the Aggregate State. *J. Am. Chem. Soc.* **2021**, *143*, 4500–4518.
- (29) Hestand, N. J.; Spano, F. C. Molecular Aggregate Photophysics beyond the Kasha Model: Novel Design Principles for Organic Materials. *Acc. Chem. Res.* **2017**, *50*, 341–350.
- (30) Balzer, F.; Kollmann, H.; Schulz, M.; Schnakenburg, G.; Lützen, A.; Schmidtmann, M.; Lienau, C.; Silies, M.; Schiek, M. Spotlight on Excitonic Coupling in Polymorphic and Textured Anilino Squaraine Thin Films. *Cryst. Growth Des.* **2017**, *17*, 6455–6466.
- (31) Zablocki, J.; Arteaga, O.; Balzer, F.; Hertel, D.; Holstein, J.; Clever, G.; Anhäuser, J.; Puttreddy, R.; Rissanen, K.; Meerholz, K.; et al. Polymorphic Chiral Squaraine Crystallites in Textured Thin Films. *Chirality* **2020**, *32*, 619–631.
- (32) Hestand, N. J.; Spano, F. C. Expanded Theory of H- and J-Molecular Aggregates: The Effect of Vibronic Coupling and Intermolecular Charge Transfer. *Chem. Rev.* **2018**, *118*, 7069–7163.
- (33) Chen, G.; Sasabe, H.; Sasaki, Y.; Katagiri, H.; Wang, X.-F.; Sano, T.; Hong, Z.; Yang, Y.; Kido, J. A Series of Squaraine Dyes: Effects of Side Chain and the Number of Hydroxyl Groups on Material Properties and Photovoltaic Performance. *Chem. Mater.* **2014**, *26*, 1356–1364.
- (34) Dirk, C.; Herndon, W.; Cervantes-Lee, F.; Selna, H.; Martinez, S.; Kalamegham, P.; Tan, A.; Campos, G.; Velez, M.; Zyss, J.; et al. Squarylium Dyes: Structural Factors Pertaining to the

- Negative Third-Order Nonlinear Optical Response. *J. Am. Chem. Soc.* **1995**, *117*, 2214–2225.
- (35) Hestand, N. J.; Zheng, C.; Penmetcha, A. R.; Cona, B.; Cody, J. A.; Spano, F. C.; Collison, C. J. Confirmation of the Origins of Panchromatic Spectra in Squaraine Thin Films Targeted for Organic Photovoltaic Devices. *J. Phys. Chem. C* **2015**, *119*, 18964–18974.
- (36) Zablocki, J.; Schulz, M.; Schnakenburg, G.; Beverina, L.; Warzanowski, P.; Revelli, A.; Grüninger, M.; Balzer, F.; Meerholz, K.; Lützen, A.; et al. Structure and Dielectric Properties of Anisotropic n-Alkyl Anilino Squaraine Thin Films. *J. Phys. Chem. C* **2020**, *124*, 22721–22732.
- (37) Zheng, C.; Bleier, D.; Jalan, I.; Pristash, S.; Penmetcha, A. R.; Hestand, N. J.; Spano, F. C.; Pierce, M. S.; Cody, J. A.; Collison, C. J. Phase separation, crystallinity and monomer-aggregate population control in solution processed small molecule solar cells. *Sol. Energy Mater. Sol.* **2016**, *157*, 366–376.
- (38) Spingler, B.; Schnidrig, S.; Todorova, T.; Wild, F. Some thoughts about the single crystal growth of small molecules. *CrystEngComm* **2012**, *14*, 751–757.
- (39) Sheldrick, G. M. A short history of SHELX. *Acta Crystallogr. A* **2008**, *64*, 112–122.
- (40) Dolomanov, O. V.; Bourhis, L. J.; Gildea, R. J.; Howard, J. A. K.; Puschmann, H. OLEX2: a complete structure solution, refinement and analysis program. *J. Appl. Crystallogr.* **2009**, *42*, 339–341.
- (41) Necas, D.; Klapetek, P. Gwyddion: an open-source software for SPM data analysis. *Cent. Eur. J. Phys.* **2012**, *10*, 181–188.
- (42) Thévenaz, P.; Ruttimann, U.; Unser, M. A Pyramid Approach to Subpixel Registration Based on Intensity. *IEEE T. Image Process.* **1998**, *7*, 27–41.
- (43) Schneider, C. A.; Rasband, W. S.; Eliceiri, K. W. NIH Image to ImageJ: 25 years of image analysis. *Nat. Methods* **2012**, *9*, 671–675.
- (44) Bernchou, U.; Brewer, J.; Midtiby, H.; Ipsen, J.; Bagatolli, L.; Simonsen, A. Texture of Lipid Bilayer Domains. *J. Am. Chem. Soc.* **2009**, *131*, 14130–14131.
- (45) Balzer, F.; Schiek, M.; Osadnik, A.; Wallmann, I.; Parisi, J.; Rubahn, H.-G.; Lützen, A. Substrate Steered Crystallization of Naphthal End-Capped Oligothiophenes into Nanowires: The Influence of Methoxy-Functionalization. *Phys. Chem. Chem. Phys.* **2014**, *16*, 5747–5754.
- (46) Rezakhaniha, R.; Agianniotis, A.; Schrauwen, J.; Griffa, A.; Sage, D.; Bouten, C.; van de Vosse, F.; Unser, M.; Stergiopoulos, N. Experimental investigation of collagen waviness and orientation in the arterial adventitia using confocal laser scanning microscopy. *Biomech. Model. Mechanobiol.* **2012**, *11*, 461–473.
- (47) DeMay, B.; Bai, X.; Howard, L.; Occipinti, P.; Meseroll, R.; Spiliotis, E.; Oldenbourg, R.; Gladfelter, A. Septin filaments exhibit a dynamic, paired organization that is conserved from yeast to mammals. *J. Cell Biol.* **2011**, *193*, 1065–1081.
- (48) Schiek, M.; Balzer, F.; Al-Shamery, K.; Lützen, A.; Rubahn, H.-G. Nanoaggregates from Thiophene/Phenylene Co-oligomers. *J. Phys. Chem. C* **2009**, *113*, 9601–9608.
- (49) Balzer, F.; Resel, R.; Lützen, A.; Schiek, M. Quasi-one-dimensional cyano-phenylene aggregates: Uniform molecule alignment contrasts varying electrostatic surface potential. *J. Chem. Phys.* **2017**, *146*, 134704.
- (50) Terenziani, F.; Painelli, A.; Katan, C.; Charlot, M.; Blanchard-Desce, M. Charge instability in quadrupolar chromophores: Symmetry breaking and solvatochromism. *J. Am. Chem. Soc.* **2006**, *128*, 15742–15755.
- (51) Sanyal, S.; Painelli, A.; Pati, S. K.; Terenziani, F.; Sissa, C. Aggregates of quadrupolar dyes for two-photon absorption: the role of intermolecular interactions. *Phys. Chem. Chem. Phys.* **2016**, *18*, 28198–28208.
- (52) Virtanen, P.; Gommers, R.; Oliphant, T. E.; Haberland, M.; Reddy, T.; Cournapeau, D.; Burovski, E.; Peterson, P.; Weckesser, W.; Bright, J.; et al. SciPy 1.0: fundamental algorithms for scientific computing in Python. *Nat. Methods* **2020**, *17*, 261–272.
- (53) Anzola, M.; Painelli, A. Aggregates of polar dyes: beyond the exciton model. *Phys. Chem. Chem. Phys.* **2021**, *23*, 8282–8291.
- (54) Funke, S.; Duwe, M.; Balzer, F.; Thiesen, P. H.; Hingerl, K.; Schiek, M. Determining the Dielectric Tensor of Microtextured Organic Thin Films by Imaging Mueller Matrix Ellipsometry. *J. Phys. Chem. Lett.* **2021**, *12*, 3053–3058.
- (55) Bay, M. M.; Vignolini, S.; Vynck, K. PyLlama: A stable and versatile Python toolkit for the electromagnetic modelling of multilayered anisotropic media. *Comput. Phys. Commun.* **2022**, *273*, 108256.
- (56) Bay, M.; Vignolini, S.; Vynck, K. PyLlama. <https://github.com/VignoliniLab/PyLlama>. Date of access: July 17, 2022.
- (57) Ramachandran, G. N.; Ramaseshan, S. In *Kristalloptik · Beugung/Crystal Optics · Diffraction*; Flügge, S., Ed.; Handbuch der Physik; Springer: Berlin, 1961; Vol. XXV/1, pp 1–217.
- (58) Tompkins, H., Irene, E., Eds. *Handbook of Ellipsometry*; William Andrew Publishing: Norwich, NY, 2005.
- (59) Dressel, M.; Gompf, B.; Faltermeier, D.; Tripathi, A. K.; Pflaum, J.; Schubert, M. Kramers-Kronig-consistent optical functions of anisotropic crystals: generalized spectroscopic ellipsometry on pentacene. *Opt. Express* **2008**, *16*, 19770.
- (60) Sturm, C.; Höfer, S.; Hingerl, K.; Mayerhöfer, T. G.; Grundmann, M. Dielectric function decomposition by dipole interaction distribution: application to triclinic  $K_2Cr_2O_7$ . *New J. Phys.* **2020**, *22*, 073041.

## □ Recommended by ACS

### Potential-Controlled Organization of 2,3-Diphenyl-5,7-di(thiophen-2-yl)thieno[3,4-b]pyrazine Adsorbed on Au(111) and Au(100) Electrodes

Shakil N. Afraj, Ming-Chou Chen, et al.

JULY 21, 2022

THE JOURNAL OF PHYSICAL CHEMISTRY C

[READ ▶](#)

### Excited State and Transient Chemistry of a Perylene Derivative (DBP). An Untold Story

Jishnudas Chakkamalayath, Prashant V. Kamat, et al.

NOVEMBER 14, 2022

THE JOURNAL OF PHYSICAL CHEMISTRY A

[READ ▶](#)

### Polarized Fluorescence of N-Salicylideneaniline Derivatives Formed by *In Situ* Exchange from N-Benzylideneaniline Side Groups in Photoaligned Liquid Crystalline Copolymer Films

Hinano Yamaguchi, Nobuhiro Kawatsuki, et al.

FEBRUARY 23, 2022

LANGMUIR

[READ ▶](#)

### Unusual Alternating Crystallization-Induced Emission Enhancement Behavior in Nonconjugated $\omega$ -Phenylalkyl Tropylum Salts

Reece D. Crocker, Thanh Vinh Nguyen, et al.

NOVEMBER 22, 2021

JOURNAL OF THE AMERICAN CHEMICAL SOCIETY

[READ ▶](#)

[Get More Suggestions >](#)